

# Localized Structural and Functional Deficits in a Nonhuman Primate Model of Outer Retinal Atrophy

Ying V. Liu,<sup>1</sup> Gregory Konar,<sup>1</sup> Kanza Aziz,<sup>1</sup> Sai Bo Bo Tun,<sup>2</sup> Candice Ho Ee Hua,<sup>2</sup> Bingyao Tan,<sup>2,3</sup> Jing Tian,<sup>4</sup> Chi D. Luu,<sup>5,6</sup> Veluchamy A. Barathi,<sup>2,7,8</sup> and Mandeep S. Singh<sup>1</sup>

<sup>1</sup>Wilmer Eye Institute, Johns Hopkins University School of Medicine, Baltimore, Maryland, United States

<sup>2</sup>Singapore Eye Research Institute, Singapore National Eye Center, Singapore, Singapore

<sup>3</sup>SERI-NTU Advanced Ocular Engineering (STANCE), Singapore, Singapore

<sup>4</sup>Department of Biostatistics, Johns Hopkins University Bloomberg School of Public Health, Baltimore, United States

<sup>5</sup>Centre for Eye Research Australia, Royal Victorian Eye and Ear Hospital, Victoria, Australia

<sup>6</sup>Ophthalmology, Department of Surgery, University of Melbourne, Victoria, Australia

<sup>7</sup>Academic Clinical Program in Ophthalmology, Duke-NUS Graduate Medical School, Singapore, Singapore

<sup>8</sup>Department of Ophthalmology, Yong Loo Lin School of Medicine, National University of Singapore, Singapore, Singapore

Correspondence: Mandeep S. Singh, Wilmer Eye Institute, Johns Hopkins University School of Medicine, 600 N. Wolfe Street, Baltimore, MD 21287, USA; [singhcorrespauth@gmail.com](mailto:singhcorrespauth@gmail.com).

YVL and GK are joint first authors, and contributed equally. VAB and MSS are joint last authors.

**Received:** December 6, 2020

**Accepted:** July 2, 2021

**Published:** October 13, 2021

Citation: Liu YV, Konar G, Aziz K, et al. Localized structural and functional deficits in a nonhuman primate model of outer retinal atrophy. *Invest Ophthalmol Vis Sci.* 2021;62(13):8. <https://doi.org/10.1167/iovs.62.13.8>

**PURPOSE.** Cell-based therapy development for geographic atrophy (GA) in age-related macular degeneration (AMD) is hampered by the paucity of models of localized photoreceptor and retinal pigment epithelium (RPE) degeneration. We aimed to characterize the structural and functional deficits in a laser-induced nonhuman primate model, including an analysis of the choroid.

**METHODS.** Macular laser photocoagulation was applied in four macaques. Fundus photography, optical coherence tomography (OCT), dye angiography, and OCT-angiography were conducted over 4.5 months, with histological correlation. Longitudinal changes in spatially resolved macular dysfunction were measured using multifocal electroretinography (MFERG).

**RESULTS.** Lesion features, depending on laser settings, included photoreceptor layer degeneration, inner retinal sparing, skip lesions, RPE elevation, and neovascularization. The intralesional choroid was degenerated. The normalized mean MFERG amplitude within lesions was consistently lower than control regions ( $0.94 \pm 0.35$  vs.  $1.10 \pm 0.27$ ,  $P = 0.032$  at month 1,  $0.67 \pm 0.22$  vs.  $0.83 \pm 0.15$ ,  $P = 0.0002$  at month 2, and  $0.97 \pm 0.31$  vs.  $1.20 \pm 0.21$ ,  $P < 0.0001$  at month 3.5). The intertest variation of mean MFERG amplitudes in rings 1 to 5 ranged from 13.0% to 26.0% in normal eyes.

**CONCLUSIONS.** Laser application in this model caused localized outer retinal, RPE, and choriocapillaris loss. Localized dysfunction was apparent by MFERG in the first month after lesion induction. Correlative structure-function testing may be useful for research on the functional effects of stem cell-based therapy for GA. MFERG amplitude data should be interpreted in the context of relatively high intertest variability of the rings that correspond to the central macula. Sustained choroidal insufficiency may limit long-term subretinal graft viability in this model.

**Keywords:** age-related macular degeneration, macular laser photocoagulation, nonhuman primate model, retinal atrophy, retinal transplantation

Geographic atrophy (GA), the hallmark retinal lesion of advanced nonexudative age-related macular degeneration (AMD), is characterized by localized degeneration of retinal pigment epithelium (RPE) and photoreceptor cells.<sup>1–5</sup> The need for GA treatment is presently unmet.<sup>6</sup> Stem cell-derived RPE transplantation is envisioned as a method of preserving vision, by regenerating the RPE layer at the border of GA lesions and protecting viable photoreceptor cells from decline.<sup>7–16</sup> Additionally, photoreceptor transplantation is a potentially complementary strategy to regenerate photoreceptor cells and improve retinal function within GA lesions.<sup>17–23</sup>

A key challenge in stem cell therapy research for GA is the scarcity of naturally occurring or transgenic animal models with localized atrophy of RPE and photoreceptor cells.<sup>24–26</sup> The term “complete RPE and outer retinal atrophy (cRORA)” was recently introduced by the Classification of Atrophy Meetings (CAM) expert panel, describing photoreceptor layer and RPE atrophy in patients with AMD based on optical coherence tomography (OCT) criteria.<sup>27</sup> This underscores the widespread recognition of photoreceptor layer and RPE atrophy as a target of future clinical trials of cellular regeneration in AMD. Among genetic mouse models, small GA-like lesions occur in aged *Ccl2*<sup>-/-</sup>, *Ccr2*<sup>-/-</sup>,<sup>28</sup>

DICER1-deficient,<sup>29,30</sup> *Ahr*<sup>-/-</sup>,<sup>31</sup> and *Elovl4*-mutant<sup>32</sup> mice. Early AMD-like changes of RPE degeneration occur in the *SOD2* knockdown model.<sup>33</sup> Nonhuman primates with naturally occurring mild or intermediate nonexudative AMD-like lesions have been described,<sup>34–38</sup> but none thus far with the cRORA-like lesions of established GA. Chemically induced retinal degeneration in rodents produced localized RPE and photoreceptor degeneration.<sup>39</sup> However, in large animals, this technique appears to cause selective photoreceptor damage while sparing the RPE cells<sup>40</sup>—possibly, a dose-dependent effect—therefore, simulating the localized degenerative phenotype of GA only partially. Mechanical induction of retinal degeneration, by placing nonpermeable material in the subretinal space, also produces photoreceptor-only loss.<sup>41</sup> Light-induced injury models<sup>42–44</sup> including verteporfin photodynamic therapy application in mice<sup>45</sup> appear to induce primarily choriocapillaris and/or RPE changes. All models other than the nonhuman primate lack a macula. Thus, they do not fully replicate the spatial localization of human GA lesions in the posterior pole of the ocular fundus. This feature is important for translational stem cell studies focused on optimizing stem cell delivery approaches to the subretinal space at the posterior pole.

The normal outer retina lacks intrinsic vasculature. Therefore, the long-term viability of subretinally transplanted therapeutic cells depends on the adequacy of the choroidal vascular supply. Data suggest that the human choroid is structurally and functionally attenuated in GA.<sup>46–50</sup> Histological and in vivo imaging data also implicate choroidal degeneration in another important cause of macular degeneration: Stargardt disease.<sup>51–58</sup> Therefore, choroidal status may be an important determinant of stem cell therapy outcomes in at least two disease indications. Recent cell transplantation studies have shown surviving subretinal cells,<sup>10,11,41,59</sup> but the impact of the choroid as a modulating factor remains poorly understood.

Greater understanding of relevant large animal models will enable further progress in cell therapy development for AMD.<sup>60</sup> Here, we aimed to determine the extent to which precise lesion features could be optimized by modulating the laser intensity and pattern characteristics. We also aimed to understand structure-function correlation and characterize the temporal evolution of localized atrophy of RPE and photoreceptor cells in the lesioned nonhuman primate macula. In addition, we considered it a priority to analyze choroidal features to address this knowledge gap in the literature.

## MATERIALS AND METHODS

### Animals

The study included four adult cynomolgus macaques (*Macaca fascicularis*), designated as subjects CM1 to CM4, that were aged 6 to 8 years (approximate human equivalent: 18–24 years<sup>61</sup>) and weighed 4 to 7 kg. All animal procedures conformed to the ARVO Statement for the Use of Animals in Ophthalmic and Vision Research and the SingHealth standard for responsible use of animals in research. The SingHealth Institutional Animal Care and Use Committee (IACUC, approval number 2015/SHS/1134) approved the study. All procedures were carried out in the SingHealth Experimental Medicine Centre, which is fully accredited by the Association for Assessment and Accreditation of Laboratory Animal Care International (AAALAC). The study proto-

col, including enrichment and caging system, was followed as per the National Advisory Committee for Laboratory Animal Research (NACLAR) guidelines. The temperature of the housing room was maintained at 25°C to 27°C and the relative humidity was kept between 45% to 55%. Equipment and toys were regularly changed. Food was provided twice daily, and water was available ad libitum. Before recruitment into the study, the animals were examined comprehensively to exclude ocular disease.

### Laser Lesion Induction

Retinal atrophy was induced by laser photocoagulation on day 0 of the experiment in one eye each of four macaques using a 532 nm green frequency-doubled Nd:Crystal laser (PurePoint 532 nm Green Laser, Alcon Laboratories, Fort Worth, TX, USA) attached to a slit-lamp delivery system. 532 nm laser is primarily absorbed by melanin-containing RPE cells causing secondary photoreceptor damage. A handheld Mainster focal/grid laser contact lens was used for the laser procedures (High-power settings: spot size 50  $\mu$ m, power 250 mW, duration 200 ms; Low-power settings: spot size 50  $\mu$ m, power 150 mW, duration 200 ms). As a reference, prior studies for CNV induction used power, spot size, and duration settings that were approximately 700 mW, 50  $\mu$ m, and 0.1 seconds.<sup>62,63</sup> Thus, our power settings were chosen to be lower than those for CNV induction. For confluent application, the burns were placed with their edges touching but not overlapping. For nonconfluent application, burns were placed about one spot size apart. Single-shot mode was used to enable the precise control of spot location and separation. Laser application settings are shown in Supplementary Table S1.

### Retinal Imaging

**Indocyanine Green Angiography (ICGA).** ICG (VERDYE, Diagnostic Green; dose 1 mg/kg) dissolved in water was administered via the intravenous route. The retinal and choroidal images were captured using scanning laser fundus imaging with high-resolution OCT Multimodal Imaging Platform (Spectralis, Heidelberg Engineering, Franklin, MA, USA). Images were obtained after dye injection at different phases as follows: early phase (0–2 minutes), midphase (4–7 minutes), and late phase (8–12 minutes onward).

**Fluorescein Angiography.** Ten percent sodium fluorescein (Curatis AG; dose 10 mg/kg) dye was given via the intravenous route. The retinal images were captured after dye injection at different phases as follows: early phase (0–3 minutes), midphase (4–8 minutes), and late phase (10–12 minutes onward) using scanning laser fundus imaging with high-resolution OCT Multimodal Imaging Platform Spectralis, Heidelberg Engineering, Heidelberg, Germany).

**Optical Coherence Tomography.** Retinal optical coherence tomography (OCT) imaging assay was performed using spectral-domain OCT (Spectralis, Heidelberg Engineering). The volume scan (20°  $\times$  20° scan, 61 B-scans per image) was captured at the laser area and nonlaser area of both eyes at baseline and months 1, 2, 3.5, and 4.5. Retinal layers were annotated based on published information<sup>64,65</sup> on the use of this modality in NHPs. Manual correction was applied to ensure the accuracy of the layer segmentation.

**OCT Angiography.** High-resolution AngioScan OCT Angiography (OCT-A) was taken using Nidek RS3000 (Nidek CO. Ltd, Gamagori, Japan) at the laser area and nonlaser area

of both eyes. Superficial vessel plexus consists of the large vessels and microvasculature within the retinal nerve fiber layer, and deep capillary plexus consists of the microvasculature within the inner plexiform layer and outer plexiform layer. Choriocapillaris was segmented from 31 to 40  $\mu\text{m}$  underneath the retinal pigment epithelium. Manual correction was applied to ensure the accuracy of the layer segmentation. Choriocapillaris flow void density was calculated based on a reported method.<sup>66</sup> The retinal perfusion density and choriocapillaris flow void density was evaluated from the  $3 \times 3$  mm high magnification scans. The retinal OCTA images were thresholded by the mean grayscale value of the image, and the perfusion density was calculated as the ratio between the vascular regions per the total imaged area.

### Multifocal Electroretinography

Multifocal electroretinography (MFERG) recordings were obtained using the RETImap system (Roland Consult, Brandenburg a.d. Havel, Germany). Jet electrodes were used to perform MFERG. The 61- and/or 103-segment stimulus protocols were used. Responses to the 61-segment test protocol were recorded at months 1, 2, and 3.5. Responses to the 103-segment test protocol were recorded only at month 3.5. The results were averages of eight cycles. The response amplitude at each locus was normalized to the baseline (average amplitude in control eyes from 1 month to 3 months) amplitude at the approximate same locus. The upper limit of normalized values was capped at 100%. Normalized amplitudes of lesion area and nonlesion area were longitudinally compared over time. The 61 segments in each eye were grouped into six rings from the center to the periphery per manufacturer's readout. The amplitude ratio of each ring was compared between lesion and control eyes. We did not analyze implicit time values because available data do not support the correlation of this metric with photoreceptor loss in photic retinal injury.

### Histopathology and Immunohistochemistry

The whole macaque eye was enucleated and fixed in 10% neutral buffered formalin solution (Leica Surgipath, Leica Biosystems Richmond, Inc., Richmond, IL, USA) for 24 hours. The eye was then dissected on the following day to remove the cornea and lens. It was then fixed again in 10% neutral buffered formalin solution (Leica Surgipath, Leica Biosystems Richmond, Inc.) for 24 hours, dehydrated in increasing concentrations of ethanol, cleared in xylene, and embedded in paraffin (Leica-Surgipath, Leica Biosystems Richmond, Inc.). Four-micron sections were cut using a rotary microtome (RM2255, Leica Biosystems Nussloch GmbH, Nussloch, Germany) and collected on POLYSINE microscope glass slides (Gerhard Menzel, Thermo Fisher Scientific, Newington, CT, USA). The sections were dried in a 37°C oven for at least 24 hours. The sections were heated on a 60°C heat plate, deparaffinized in xylene, and rehydrated in decreasing concentrations of ethanol. Hematoxylin and eosin (H&E) staining was performed according to a standard procedure. A light microscope (Axioplan 2; Carl Zeiss Meditec GmbH, Oberkochen, Germany) was used to examine the slides and capture the images.

In parallel, colocalization immunofluorescence staining was performed. Antigen retrieval was performed by incubating slides in sodium citrate buffer (10 mM sodium citrate, 0.05% Tween 20, pH 6.0) for 20 minutes at 95°C to 100°C and

then cooling the slides down for 20 minutes at room temperature (RT). The sections were then washed three times for 5 minutes each with 1X PBS. Nonspecific sites were blocked with a 5% goat serum solution containing 2% bovine serum albumin (BSA) and 0.1% Triton X-100 in 1X PBS for 1 hour at RT in a humidified chamber. The primary antibodies shown in Supplementary Table S2 were diluted in 1X PBS and applied and incubated overnight at 4°C in a humid chamber. After washing the slides twice with 1X PBS and once with 1X PBS containing 0.1% Tween for 10 minutes each, corresponding secondary antibodies (conjugated with Alexa 594; Molecular Probes, Eugene, OR, USA) were applied at a concentration of 1:1000 in 1X PBS and incubated for 90 minutes at RT as shown in Supplementary Table S2. The slides were then washed twice with 1X PBS and once with 1X PBS containing 0.1% Tween for 5 minutes each. The slides were mounted with Prolong Diamond Antifade Reagent and DAPI (Invitrogen, Eugene, Oregon, USA) to visualize cell nuclei. For negative controls, the primary antibody was omitted. A fluorescence microscope (Axioplan 2; Carl Zeiss Meditec GmbH) was used to examine the slides and capture the images. Experiments were repeated in duplicate for antibody staining.

### Data Analysis

MFERG amplitude data were analyzed using the generalized estimating equation (GEE) model, variance correction (jackknife variance estimator), considering the repeated measures for two eyes in the same animal and the multiple loci measured per time point per eye. Coefficients of variation were calculated by dividing the means of the repeated measurement by the standard deviation of those means.

### RESULTS

We modulated the overall laser intensity in terms of spot power (high versus low) and spot separation (confluent versus nonconfluent) (Supplementary Fig. S1). The appearance of the retina after low-power and high-power application is shown in Figure 1. Confluent application resulted in lesions that were immediately contiguous by biomicroscopic observation (Figs. 1a'-b"). With nonconfluent application, we placed the laser spots approximately one spot size apart initially. However, by 15 minutes postapplication, the penumbra of individual burns had expanded (Figs. 1d' and d"). By 4.5 months, the pigmented lesions' edges appeared indistinct (Figs. 1e' and e"). We observed pigmentary changes on fundus photos at all laser intensity settings. Pigmentary reaction, including hypo- and hyperpigmentation, was especially marked with high-power laser applied at confluence (Fig. 1b").

Lesions showed atrophic or neovascular characteristics, depending on laser intensity (Fig. 2). Confluent and nonconfluent application produced predominantly atrophic lesions as long as the power was kept low. Features indicating atrophy included reduced fluorescence due to hypoperfusion, fluorescence blockage due to intraretinal hyperpigmentation, and fluorescence transmission windows due to RPE atrophy or depigmentation (Figs. 2a' and b'). Focal areas of fluorescein leakage indicated that choroidal neovascularization (CNV), when present, occupied a minor proportion of total lesion area (Fig. 2a'). High-power laser application produced significant fluorescein leakage by 4.5 months,

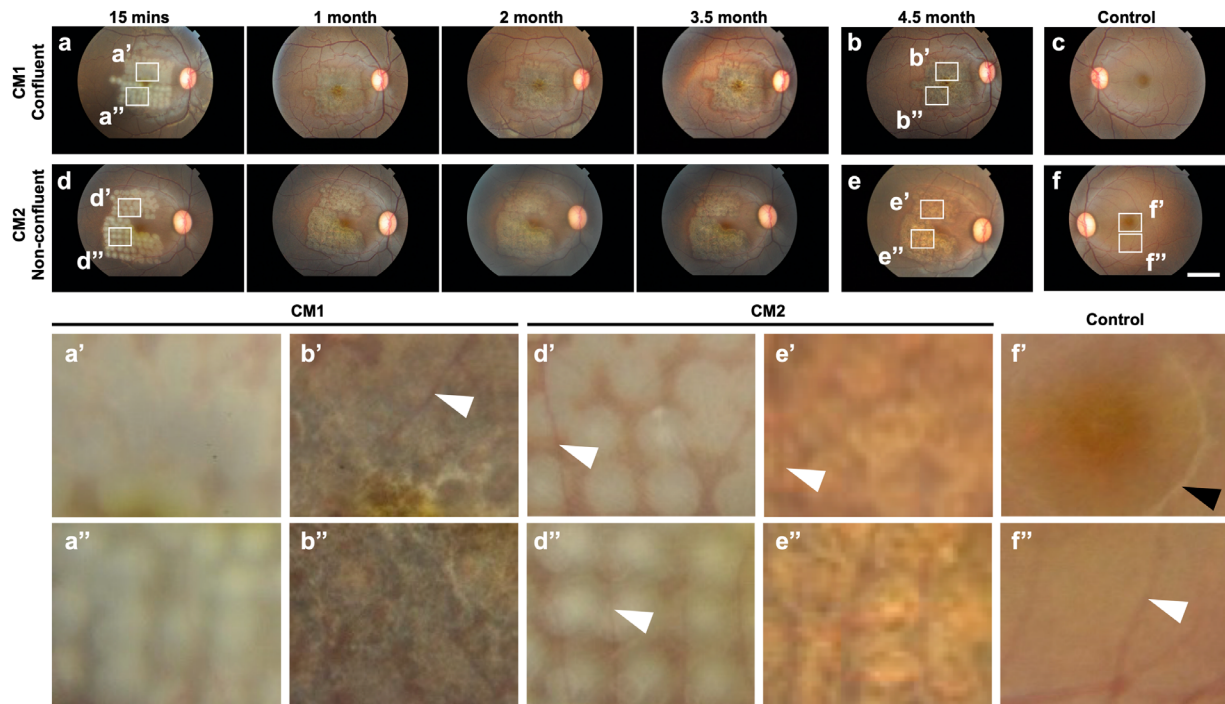


**FIGURE 1.** Evolution of pigmentary changes over 4.5 months. **a.** Images of the right fundus from 15 minutes to 3.5 months after laser application in a confluent pattern (subject CM1). **b.** Outcome image of the right fundus 4.5 months after confluent laser application in subject CM1. **c.** Control left fundus without laser application (subject CM1). **d.** Images of the fundus from 15 minutes to 3.5 months after laser application in a nonconfluent pattern in subject CM2. **e.** Outcome image of the right fundus 4.5 months after nonconfluent laser application in subject CM2. **f.** Control left fundus without laser application (subject CM2). *Scale bar* (2 mm) applies to **a–f**. 10× magnification of the *white squares*: 15-minute and 4.5-month images of low-power (**a'** and **b'**) and high-power (**a''** and **b''**) confluent laser application in CM1. 15-minute and 4.5-month images of low-power (**d'** and **d''**) and high-power (**d''** and **d''**) nonconfluent laser application in subject CM1. Foveal (**f'**) and perifoveal (**f''**) control images of CM2 showing normal macular pigmentation. Retinal blood vessels are indicated by *white arrowheads*. The perifoveal inner retinal light reflex is indicated by the *black arrowhead*.

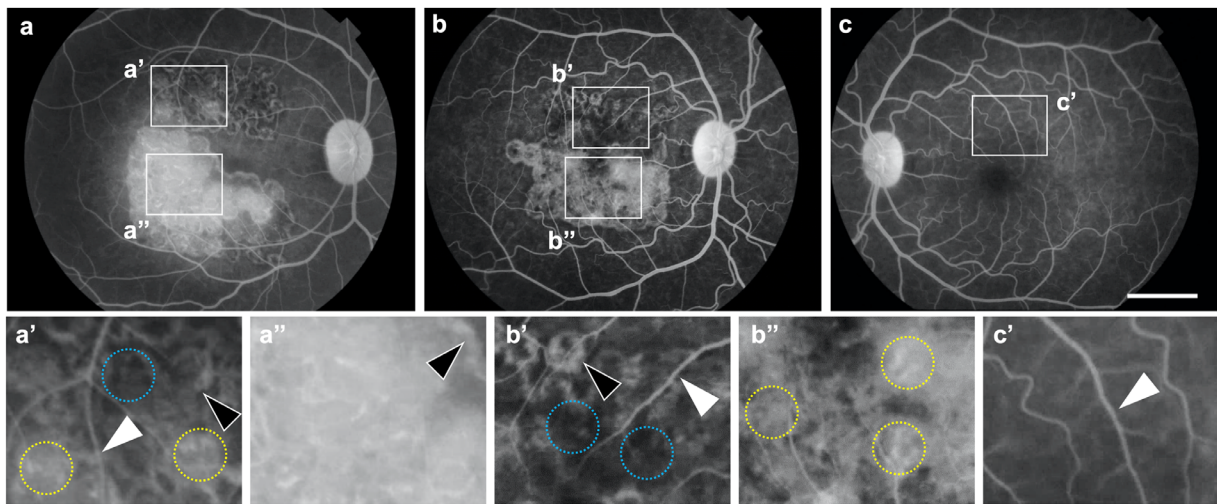


**FIGURE 2.** Development of choroidal neovascularization (CNV) with intense laser. **a.** Late fluorescein angiogram of the lesioned right fundus of subject CM2 after nonconfluent laser application at low (**a'**) and high power (**a''**). **b.** Late fluorescein angiogram of the lesioned right fundus of subject CM1 after confluent laser application at low (**b'**) and high power (**b''**). **c.** Control left fundus of subject CM1. *Scale bar* (2 mm) applies to **a–c**. 5× magnification of *white squares*: Lower power, whether applied in a nonconfluent (**a'**) or confluent (**b'**) pattern, produced hypofluorescence (*blue circles* in **a'** and **b'**). Well-demarcated late hyperfluorescent areas (*black arrowheads* in **a'** and **b'**) indicated fluorescence transmission windows due to RPE atrophy. Focal (*yellow circles* in **a'** and **b''**) or diffuse (**a''**) fluorescein leakage indicated the formation of active CNV as a result of using higher power. A control area of perifoveal retina without laser lesions is shown in **c'**. Retinal blood vessels are indicated by *white arrowheads* in **a'**, **b'**, and **c'**.

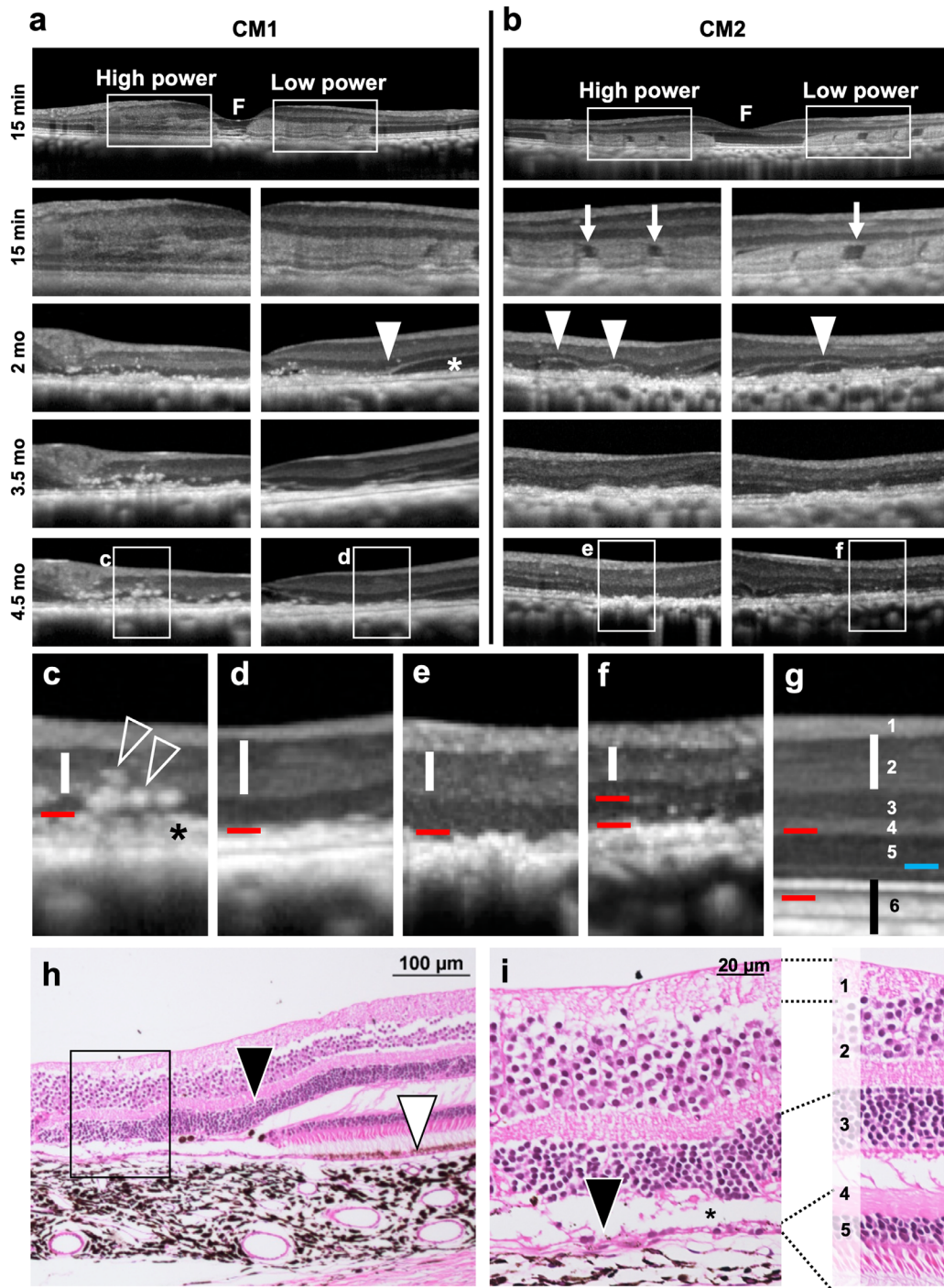


**FIGURE 3.** Photoreceptor layer and retinal pigment epithelium (RPE) changes. **a.** Serial macular optical coherence tomography (OCT) after confluent laser application, taken across areas of high- and low-power laser application in subject CM1 (F in *top row* indicates the location of the fovea). At 2 months, with low-power laser application, a sharp demarcation (*arrowhead, third row*) separated lesioned and nonlesion areas. The hyporeflective outer nuclear layer (ONL) band (*white asterisk*) was present at the nonlesion area. **b.** Serial macular OCT after nonconfluent laser application, taken across areas of high- and low-power laser application in subject CM2, through the fovea (*arrowhead, top row*). Nonconfluent laser results in skip areas between individual laser burns (*arrows, second row*). In the skip areas, ONL was relatively preserved (*arrowheads, third row*, images are not coregistered). The lesions continued to evolve through month 3.5 and showed incomplete ONL ablation by 4.5 months. **c.** High-magnification image of confluent high-power laser application outcome at 4.5 months. Intraretinal hyperreflective foci (*empty arrowheads*) were present, and the photoreceptor layer was ablated (*red line*). *Black asterisk* denotes RPE elevation/thickening. **d.** High-magnification image of confluent low-power laser application outcome at 4.5 months. The photoreceptor layer was selectively ablated (*red line*). **e.** High-magnification image of nonconfluent high-power laser application outcome at 4.5 months. The photoreceptor layer was selectively ablated (*red line*). **f.** High-magnification image of nonconfluent low-power laser application outcome at 4.5 months. The photoreceptor layer was incompletely ablated (between *red lines*). **g.** Control perifoveal retina, showing the physiological lamination pattern. 1: retinal nerve fiber layer, 2 (*vertical white lines in c–g*): ganglion cell layer and inner plexiform layer complex, 3: inner nuclear layer, 4: outer plexiform layer, 5: ONL, 6: hyperreflective bands corresponding to (from top to bottom) the ellipsoid zone (EZ), retinal pigment epithelium–Bruch’s membrane, and choriocapillaris complex. *Blue line*: external limiting membrane. *Red lines*, when separated,

indicate the photoreceptor layer including the outer nuclear layer and the inner and outer segments layers. *Single red lines* denote the outer retinal surface, that is, the position of subretinal space, when the photoreceptor layer was absent due to complete ablation. **h.** H&E stain of a transition zone (*black arrowhead*) at the border of laser-induced atrophy, similar to that depicted in **(a)**, *third row, right panel*. Normal pigmented RPE layer is shown with a *white arrow*. *Black box* magnified in **(i)**, showing loss of the normal pigmented RPE layer (*arrowhead*) and photoreceptor layer atrophy (*asterisk*). The *right panel* is a control retinal section showing the normal laminated structure, annotated 1–5, corresponding to the layers in panel **(g)**. *Scale bar*, 20  $\mu\text{m}$ , applies to both images in **(i)**.

indicating the presence of large and active CNV (Figs. 2a" and b").

Retinal thickening occurred immediately after laser application (Fig. 3 and Supplementary Fig. S2). Subsequent retinal thinning stabilized between 2 and 4.5 months (Fig. 3). We did not quantify inner versus outer retinal thinning in this dataset due to the small number of animals. Confluent laser application produced broad areas of photoreceptor layer ablation, relatively sparing the inner retina. Skip lesions, that is, areas of photoreceptor ablation alternating with spared areas, occurred with nonconfluent applications. The presence of skip lesions correlated with incomplete photoreceptor layer ablation at 4.5 months (Figs. 3e–f). High-power laser application produced intraretinal hyperreflective foci that may correspond to intraretinal pigment-laden cells on histology, although more precise anatomical correlation is required to validate this assumption (Supplementary Fig. S3). Local RPE elevation and/or subjective thickening (Figs. 3a and c) further supported the presence of CNV with high-power confluent laser application. Low-power application caused less RPE thickening and/or elevation than high power. Immunohistology subsequently confirmed photoreceptor and RPE layer damage (Figs. 3h–i and Supplementary Fig. S4). The inner retina was relatively preserved despite laser-induced atrophy of the photoreceptor layer. As this is a small dataset, representative histology from all animals (CM1–CM4) are shown in Supplementary Figs. S3 and S4.

Laser-induced GA lesions in this model showed reduced choroidal vascular perfusion on indocyanine green (ICG) and OCT angiography (Figs. 4a–d). Choroidal neovascularization was faintly visible on ICG angiography (Fig. 4e) and more clearly seen on OCT angiography (Fig. 4i). The choroidal vascular loss involved the choriocapillaris in all animals and relatively spared the larger choroidal vessels (Fig. 4b shows CM3 and g–i show CM4). Retinal vasculature remained relatively intact. Retinal perfusion density and choriocapillaris flow void density quantification are shown in Supplementary Table S3. These in vivo imaging findings were supported by histology showing choriocapillaris attenuation and relative preservation of large choroidal vessels (Figs. 4i–j). We detected evidence of choriocapillaris damage at all laser intensity settings included in this study.

Multifocal electroretinography (MFERG) provided a quantitative readout of localized retinal function. Qualitatively, the spatial distribution of dysfunctional loci in the lesioned eyes showed a center-surround pattern in general, with central response reduction and peripheral preservation (Fig. 5). We saw intertest variability in lesion and control eyes. The 103-segment readout was noisier than the 61-segment readout in one subject, CM4.

We assigned responses as being inside or outside the lesion area by referring to the infrared reflectance images that showed the lesion boundary clearly (Fig. 6a). With the 61-segment protocol, the mean normalized response amplitude in the lesions was lower than responses outside the lesions in the same eye, at all time points tested ( $0.94 \pm 0.35$

vs.  $1.10 \pm 0.27$ ,  $P = 0.032$  at month 1,  $0.67 \pm 0.22$  vs.  $0.83 \pm 0.15$ ,  $P = 0.0002$  at month 2, and  $0.97 \pm 0.31$  vs.  $1.20 \pm 0.21$ ,  $P < 0.0001$  at month 3.5). With the 103-segment protocol, the mean normalized response amplitude in lesions was lower than the nonlesion area in the same eye ( $0.79 \pm 0.27$  vs.  $0.94 \pm 0.23$ ,  $P = 0.032$  at month 3.5) (Fig. 6b).

We also studied the feasibility and utility of an unbiased approach to MFERG analysis. In this approach, we did not designate responses as being located inside or outside lesions, but instead categorized them into concentric rings per the manufacturer's software. This method could be useful for investigators when normalization is impossible, such as when both eyes are lesioned, or when preleser readings are not available. We adapted a method that has been used to evaluate toxic maculopathy in patients taking hydroxychloroquine.<sup>67</sup> This method is based on the pattern of hydroxychloroquine-induced retinal damage that selectively involves the perifoveal retina during the early stages, sparing the macular periphery. We normalized the mean ring 2 (R2) amplitude, reflecting central responses, to either ring 4 (R4) or ring 5 (R5), reflecting responses in the macular periphery. Thus, we derived the R2/R4 and R2/R5 ratios in each eye. R2/R4 and R2/R5 ratios were generally lower in lesioned eyes compared to the fellow control eyes almost (R2/R4:  $1.16 \pm 0.38$  vs.  $1.63 \pm 0.46$ ,  $P = 0.046$  at month 1,  $0.84 \pm 0.19$  vs.  $1.43 \pm 0.67$ ,  $P = 0.14$  at month 2, and  $0.83 \pm 0.21$  vs.  $1.74 \pm 0.58$ ,  $P = 0.014$  at month 3.5; R2/R5:  $1.09 \pm 0.42$  vs.  $1.58 \pm 0.45$ ,  $P < 0.0001$  at month 1,  $0.78 \pm 0.21$  vs.  $1.22 \pm 0.48$ ,  $P = 0.035$  at month 2, and  $0.79 \pm 0.24$  vs.  $1.64 \pm 0.40$ ,  $P = 0.0056$  at month 3.5). We also calculated MFERG ratios based on ring 1 amplitudes (instead of ring 2), that is, R1/R4 and R1/R5. Both R1/R4 and R1/R5 differed between lesion and control eyes at months 1 and 2 (Supplementary Fig. S5).

In this dataset, we had obtained MFERG results in normal eyes on five occasions (OD and OS preleser, and OS at months 1, 2, and 3.5), using the 61-segment protocol. We used these data to estimate the intertest variation of the 61-segment MFERG assay in nonlesioned nonhuman primate eyes. The coefficients of variation (CV) of the mean amplitudes of R1, R2, R3, R4, and R5 in nonlaser eyes ( $n = 5$ ) were 26.0%, 21.5%, 17.8%, 13.0%, and 13.8%, respectively, as shown in the Table.

## DISCUSSION

The data demonstrate that laser-induced GA-like lesions in nonhuman primates can be characterized in depth by serial in vivo retinal testing over time. We found that lesions evolved for several weeks before reaching a stable anatomical configuration. We validated the use of MFERG to measure localized functional deficits topographically, identifying the importance of mitigating intertest variation. We also present novel information regarding choriocapillaris loss in this GA model.

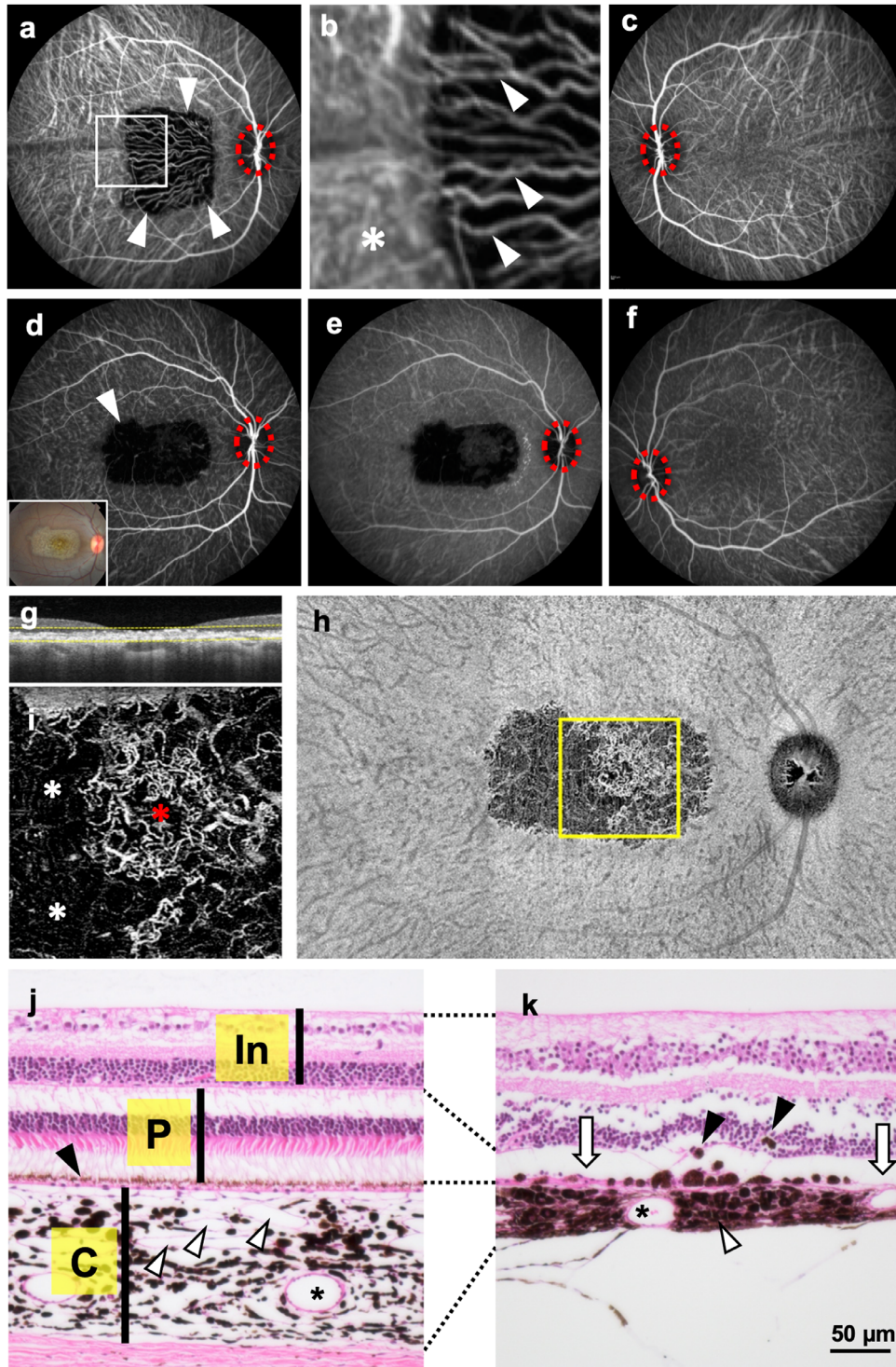


**FIGURE 4.** Choriocapillaris loss in the nonhuman primate model of geographic atrophy. **a.** Indocyanine green angiogram (ICGA) showed decreased cyanescent signal in the lasered region (boundaries denoted by *arrowheads*) in subject CM3. **b.** 4× magnification of *white square* in **(a)** showed the relative preservation of large choroidal vessels (*arrowheads*) at the laser site, compared to the relatively normal cyanescent signal in the adjacent retina (*asterisk*) of subject CM3. **c.** Control left eye of subject CM3, late phase. **d.** Early phase ICGA showing choroidal hypoperfusion (*arrowhead*) corresponding to the area of laser application that was visible biomicroscopically (*inset*). This ICGA was obtained 3.5 months after laser application in subject CM4. **e.** Late phase ICGA showed faint late hypercyanescence (*arrowhead*) within the lesion. **f.** Control left eye of the same animal, early phase ICGA. **g–i.** Optical coherence tomography angiogram (OCTA) showed choriocapillaris degeneration (*white asterisks*), relatively preserved large choroidal vessels, and choroidal neovascularization (surrounding the *red asterisk*) within the lesion area (*yellow box* in **h** is enlarged in **i**). **j.** Hematoxylin & eosin (H&E) stain of control retina. Inner retina (In), photoreceptor (P), and choroidal (C) layers are intact. The melanin-pigmented retinal pigment epithelium (RPE) layer, smaller choroidal vessels (*white arrowheads*), and retinal pigment epithelium are shown (*black arrowhead*). A large choroidal vessel is denoted with the *asterisk*. **k.** H&E-stained retina after laser application, showing total photoreceptor layer loss. The choroid (*white arrowhead*) is severely reduced in thickness and is hyperpigmented, The smaller choroidal vessels are lost and the larger choroidal vessels (*asterisk*) are relatively preserved. Pigment-

laden cells are globular and hyperpigmented, and show intraretinal migration (*black arrowheads*). The RPE layer was completely absent in parts (*white arrows*). Scale bar, 50  $\mu\text{m}$  for **f–g**. Red circles denote the optic nerve head.

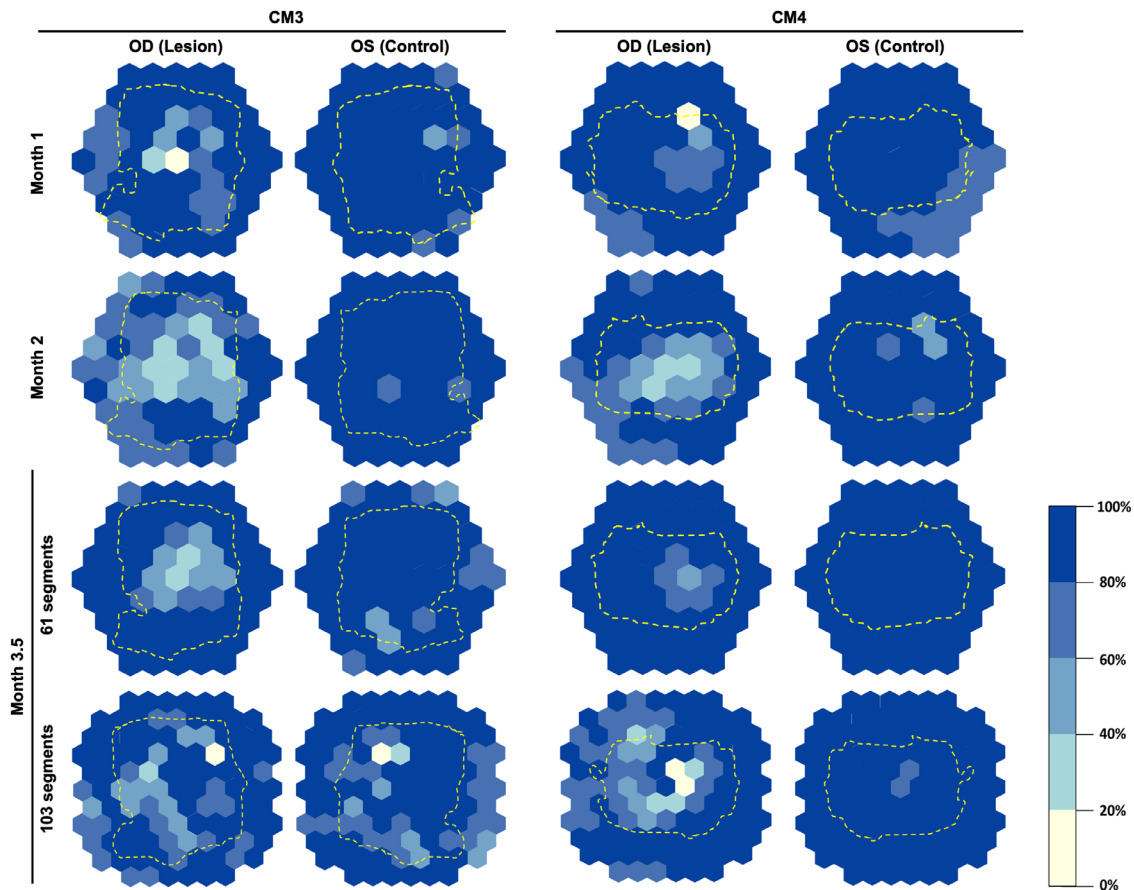


**FIGURE 5.** Spatial distribution of multifocal electroretinogram response amplitudes showing localized macular dysfunction in lesioned eyes. Color-coded heat maps showing normalized multifocal electroretinogram (MFERG) amplitudes at each test locus, for subjects CM3 and CM4, over serial testing. Right eyes (OD) were lesioned and left eyes (OS) are presented as nonlesion controls at each time point. Lesion boundaries in each right eye are denoted by *yellow dashed lines* and are laterally reflected into each left eye to indicate the contralateral lesion equivalent area.

It is well known that laser application outcomes in animal models, including CNV formation, can be unpredictable. In this experiment, confluent low-power application produced optimal results, including: 1. photoreceptor layer ablation sparing the inner retina, 2. absence of skip areas, 3. minimal CNV formation, and 4. acceptable interval to lesion stabilization. In a laser-induced C57BL/6J mouse model, 810 nm diode laser application (60-second application per spot) produced mild to severe lesions, depending on the power delivered in each case.<sup>68</sup> In that study by Ibbett and colleagues, full-field ERG amplitudes were affected, presumably because the lesions occupied a large portion of the total retinal area in mice and thus reduced the summed retinal response. In this study, manual application of laser spots produced uneven spacing. In humans, AMD does not produce significant full-field ERG deficits,<sup>69</sup> due to the small lesion size relative to total retina and the lack of panretinal photoreceptor dysfunction. Therefore, we did not evaluate full-field ERG responses in this study.

In GA lesions of nonexudative AMD, the inner nuclear and ganglion cell layers are relatively preserved despite

advanced photoreceptor and RPE atrophy.<sup>4,70,71</sup> We found it possible to selectively ablate the photoreceptor layer by carefully titrating laser intensity. Factors other than power are known to influence laser energy absorption and thermal cell damage. RPE and choroidal melanin pigmentation, and the orthogonality of the laser beam to the curvature of the posterior pole, varied considerably between animals in this study. Placing a test spot in a noncentral location can be a useful method of titrating the power before GA lesion induction. Caution should be exercised to avoid heavy laser application in a GA model. As we found in this study, excessive laser intensity is known to produce CNV,<sup>62</sup> which is undesirable in a GA model.

In human GA, evidence suggests that the choriocapillaris is degenerated and hypoperfused to some extent.<sup>46–49,72–77</sup> In macular atrophy secondary to Stargardt disease, the choriocapillaris appears to be severely attenuated.<sup>46–48,51–58,78</sup> Therefore, the laser-induced nonhuman primate GA model may also be relevant for preclinical retinal stem cell research in Stargardt disease.<sup>79,80</sup> It may be possible to avoid or reduce choriocapillaris damage in this model by changing

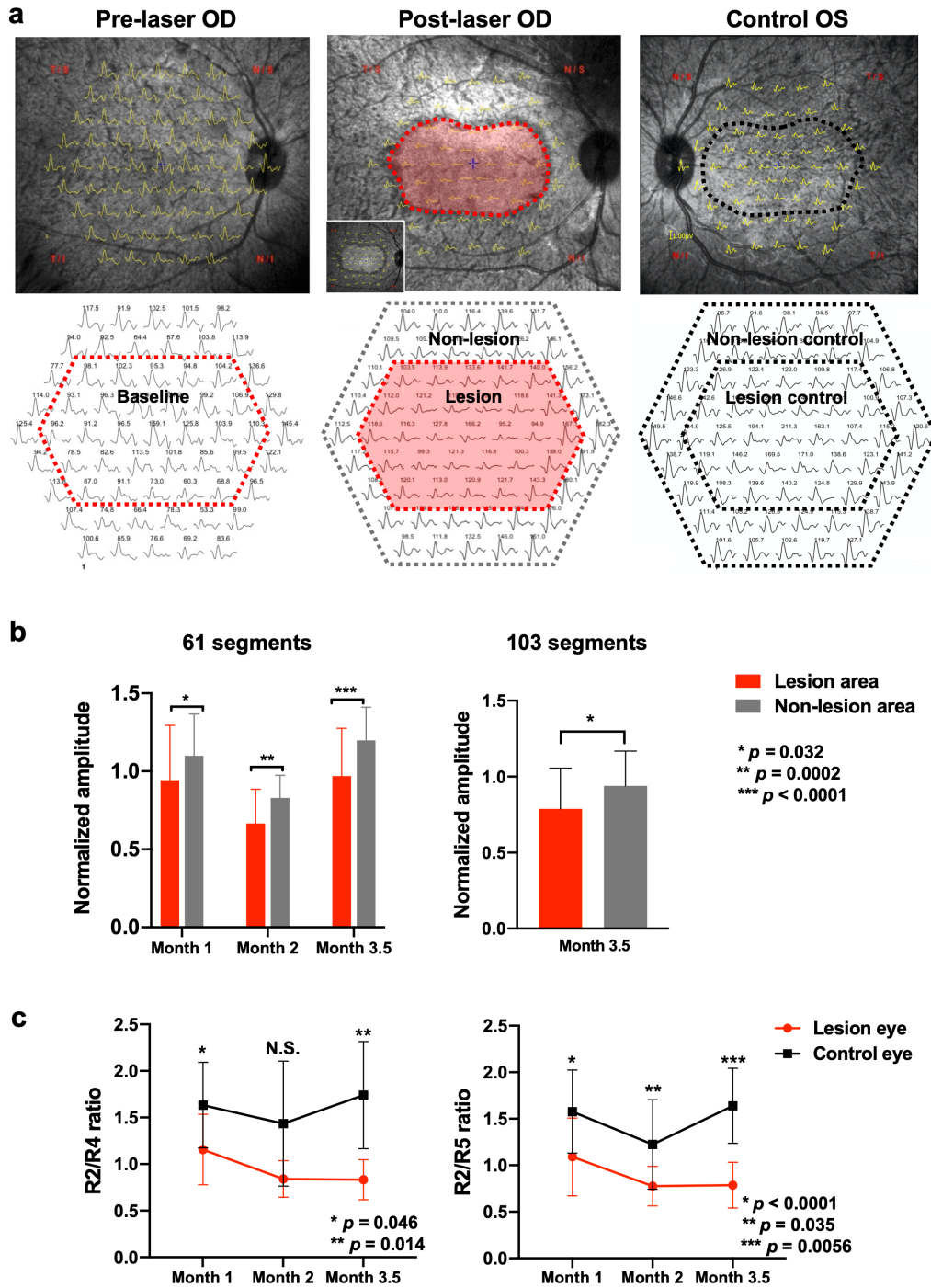


**FIGURE 6.** Consistency of multifocal electroretinogram (MFERG) response reduction in GA lesions. **a.** Infrared reflectance reference images of subject CM4 of the pre-laser right eye (OD), postlaser OD at month 3.5, and control left eye (OS) at month 3.5, with registered overlay of multifocal electroretinogram (MFERG) tracings. Red-shaded area in the post-laser OD image delineates the GA lesion boundaries and identifies traces designated as “lesion” (red boundary with shading) or “non-lesion” (outside red-shaded area, within grey line) in that eye. The equivalent control region (lateral mirror image, black line) in the OS was demarcated for normalization purposes. *Inset* shows postlaser OD retina at 3.5 months without lesion boundary markup. **b.** Mean normalized MFERG response amplitudes in the lesion and nonlesion areas at months 1, 2, and 3.5 ( $n = 4$  animals, CM1–4). Data using the 61-segment MFERG stimulus were obtained at all three time points. The 103-segment stimulus protocol was used at month 3.5 only. **c.** MFERG ring amplitude ratios (mean  $\pm$  standard deviation) over time, comparing lesion eyes to the fellow control eyes ( $n = 4$  animals, CM1–4), without fellow-eye normalization. R2, R4, and R5 denote rings 2, 4, and 5, respectively.

certain laser parameters. For example, micropulse laser exhibits selective thermal localization.<sup>11,81–83</sup> In the rabbit

model of sodium iodate injection, photoreceptor and RPE loss was accompanied by dose-dependent choroidal

**TABLE.** The Statistical Description of the MFERG Amplitudes in Nonlaser Eyes

	Ring 1	Ring 2	Ring 3	Ring 4	Ring 5
Values (n)	5	5	5	5	5
Mean	197.8	143.3	106.9	99.36	109.8
Standard deviation	51.40	30.83	19.03	12.90	15.11
Coefficient of variation (%)	25.99%	21.51%	17.80%	12.98%	13.76%

atrophy.<sup>59</sup> Rat and rabbit choriocapillaris appear to regenerate spontaneously following injury,<sup>84,85</sup> although it is unclear if this regenerative capacity exists in the primate choroid.

MFERG is an objective assay of localized macular dysfunction. Its use in this context has been validated in a nonhuman primate model with naturally occurring bilateral macular dystrophy.<sup>25</sup> MFERG has also been used to map retinal function in the visual streak of the pig model<sup>11</sup> and in the wild-type primate macula.<sup>16</sup> Notably, in our study, MFERG amplitudes in the lesions were not reduced to the same extent as is typically found in the absolute scotomas of established human GA. Full-field ERG, as a summed retinal response,<sup>24,34,86,87</sup> is poorly suited to detect and quantify localized functional deficits. This study was not adequately powered to statistically compare MFERG amplitudes between laser settings; the data here may be used to design a larger study for this purpose.

The CVs of R1, R2, and R3 were above the typically acceptable limit of intertest variability, that is, 15%. In the 61-segment protocol, the number of test loci in R1, R2, R3, R4, and R5 are 1, 6, 12, 18, and 24, respectively. Therefore, there may be a higher tolerance for variation (due to inconsistent stimulus centration) in the peripheral rings (R4 and R5) than in the central rings (R1–R3). One strategy to minimize ocular drift during the MFERG is by administering a periorbital local anesthetic injection. The potential for inconsistent centration, and therefore the central CVs, may be even higher after laser application, by the absence of normal foveal landmarks. Researchers could consider determining the CV of control and test loci that is specific to their experimental conditions.

Human GA is associated with several important molecular abnormalities, including complement activation and lipofuscin accumulation. Bruch's membrane senescence,<sup>88,89</sup> glial cell infiltration,<sup>90,91</sup> and inner retinal remodeling are important facets of GA with relevance to cell therapy. In particular, the health of Bruch's membrane may be a key determinant of cell transplantation efficacy in humans, as it influences transplanted RPE cell adherence and viability.<sup>92,93</sup> We did not study those aspects in this relatively small project wherein our resources were focused on serial in vivo evaluation. This model is also limited in that it does not demonstrate the long-term progression of atrophy that is typical of human disease. Furthermore, photochemical or oxidative damage models may reflect the molecular pathophysiology of GA compared to the presumably predominantly photothermal effect of the model reported here.

## CONCLUSIONS

Laser-induced macular degeneration in this nonhuman primate model resulted in photoreceptor, RPE, and choriocapillaris loss. The use of OCT, OCTA, dye angiography, and MFERG enabled the spatiotemporal correlation of localized structural and functional deficits in vivo. The lesion features

in this model are similar to those of cRORA as defined by the CAM expert panel. With further optimization, this model could provide a useful platform to validate stem cell-derived RPE and photoreceptor cell transplantation approaches for retinal regeneration in AMD. Given the high intertest variability of MFERG data, it is important to ascertain the magnitude of variability for the different experimental conditions specific to each laboratory. MFERG change data in the fovea and perifovea should be interpreted in the context of the high variability of the ring amplitudes that correspond to those loci. Choroidal insufficiency, if sustained, may limit the long-term viability and functionality of subretinal cellular grafts in this model.

## Acknowledgments

The authors thank Laura Frishman, PhD (University of Houston, TX), for her helpful input.

Supported by NIH R01 EY033103-01, the Foundation Fighting Blindness (Career Development Award CD-RM-0918-0749-JHU to MSS), The Shulsky Foundation, Juliette RP Vision Foundation, NEI Core Grant (EY001765), Joseph Albert Hekimian Fund, and Singapore NMRC Centre Grant (NMRC/CG/M010/2017/PreClinical).

Disclosure: **Y.V. Liu**, None; **G. Konar**, None; **K. Aziz**, None; **S.B.B. Tun**, None; **C.H.E. Hua**, None; **B. Tan**, None; **J. Tian**, None; **C.D. Luu**, None; **V.A. Barathi**, None; **M.S. Singh**, None

## References

- Keenan TD, Agrón E, Domalpally A, et al. Progression of geographic atrophy in age-related macular degeneration: AREDS2 report number 16. *Ophthalmology*. 2018;125(12):1913–1928.
- Ferris 3rd FL, Wilkinson CP, Bird A, et al. Clinical classification of age-related macular degeneration. *Ophthalmology*. 2013;120(4):844–851.
- Bird AC, Phillips RL, Hageman GS. Geographic atrophy: a histopathological assessment. *JAMA Ophthalmol*. 2014;132(3):338–345.
- Kim SY, Sadda S, Humayun MS, de Juan E, Jr., Melia BM, Green WR. Morphometric analysis of the macula in eyes with geographic atrophy due to age-related macular degeneration. *Retina*. 2002;22(4):464–470.
- Green WR, Key SN, 3rd. Senile macular degeneration: a histopathologic study. *Trans Am Ophthalmol Soc*. 1977;75:180–254.
- Singh MS, MacLaren RE. Stem cell treatment for age-related macular degeneration: the challenges. *Invest Ophthalmol Vis Sci*. 2018;59(4):Amd78–amd82.
- Ben M, Berek K, Habeler W, Plancheron A, et al. Human ESC-derived retinal epithelial cell sheets potentiate rescue of photoreceptor cell loss in rats with retinal degeneration. *Sci Transl Med*. 2017;9(421).
- Kashani AH, Lebkowski JS, Rahhal FM, et al. A bioengineered retinal pigment epithelial monolayer for advanced, dry age-related macular degeneration. *Sci Transl Med*. 2018;10(435):eaao4097.
- da Cruz L, Fynes K, Georgiadis O, et al. Phase 1 clinical study of an embryonic stem cell-derived retinal pigment epithelium patch in age-related macular degeneration. *Nat Biotechnol*. 2018;36(4):328–337.
- Mandai M, Watanabe A, Kurimoto Y, et al. Autologous induced stem-cell-derived retinal cells for macular degeneration. *N Engl J Med*. 2017;376(11):1038–1046.

11. Sharma R, Khristov V, Rising A, et al. Clinical-grade stem cell-derived retinal pigment epithelium patch rescues retinal degeneration in rodents and pigs. *Sci Transl Med.* 2019;11(475):eaat5580.
12. Schwartz SD, Tan G, Hosseini H, Nagiel A. Subretinal transplantation of embryonic stem cell-derived retinal pigment epithelium for the treatment of macular degeneration: an assessment at 4 years. *Invest Ophthalmol Vis Sci.* 2016;57(5):ORSFc1-ORSFc9.
13. Idelson M, Alper R, Obolensky A, et al. Immunological properties of human embryonic stem cell-derived retinal pigment epithelial cells. *Stem Cell Rep.* 2018;11(3):681-695.
14. Davis RJ, Alam NM, Zhao C, et al. The developmental stage of adult human stem cell-derived retinal pigment epithelium cells influences transplant efficacy for vision rescue. *Stem Cell Rep.* 2017;9(1):42-49.
15. Stanzel BV, Liu Z, Somboonthanakij S, et al. Human RPE stem cells grown into polarized RPE monolayers on a polyester matrix are maintained after grafting into rabbit subretinal space. *Stem Cell Rep.* 2014;2(1):64-77.
16. Ben M, Berek K, Bertin S, Brazhnikova E, et al. Clinical-grade production and safe delivery of human ESC derived RPE sheets in primates and rodents. *Biomaterials.* 2020;230:119603.
17. Singh MS, Charbel Issa P, Butler R, et al. Reversal of end-stage retinal degeneration and restoration of visual function by photoreceptor transplantation. *Proc Natl Acad Sci USA.* 2013;110(3):1101-1106.
18. Lamba DA, McUsic A, Hirata RK, Wang PR, Russell D, Reh TA. Generation, purification and transplantation of photoreceptors derived from human induced pluripotent stem cells. *PLoS One.* 2010;5(1):e8763.
19. Mandai M, Fujii M, Hashiguchi T, et al. iPSC-derived retina transplants improve vision in rd1 end-stage retinal degeneration mice. *Stem Cell Reports.* 2017;8(1):69-83.
20. Kwan ASL, Wang S, Lund RD. Photoreceptor layer reconstruction in a rodent model of retinal degeneration. *Exp Neurol.* // 1999;159(1):21-33.
21. Pearson RA, Barber AC, Rizzi M, et al. Restoration of vision after transplantation of photoreceptors. *Nature.* 2012;485(7396):99-103.
22. Tucker BA, Park I-H, Qi SD, et al. Transplantation of adult mouse iPS cell-derived photoreceptor precursors restores retinal structure and function in degenerative mice. *PLoS One.* 2011;6(4):e18992.
23. Yang Y, Mohand-Said S, Leveillard T, Fontaine V, Simonutti M, Sahel JA. Transplantation of photoreceptor and total neural retina preserves cone function in P23H rhodopsin transgenic rat. *PLoS One.* 2010;5(10):e13469.
24. Moshiri A, Chen R, Kim S, et al. A nonhuman primate model of inherited retinal disease. *J Clin Invest.* 2019;129(2):863-874.
25. Dominik Fischer M, Zobor D, Keliris GA, et al. Detailed functional and structural characterization of a macular lesion in a rhesus macaque. *Doc Ophthalmol.* 2012;125(3):179-194.
26. Ikeda Y, Nishiguchi KM, Miya F, et al. Discovery of a cynomolgus monkey family with retinitis pigmentosa. *Invest Ophthalmol Vis Sci.* 2018;59(2):826-830.
27. Sadda SR, Guymer R, Holz FG, et al. Consensus definition for atrophy associated with age-related macular degeneration on OCT: classification of atrophy report 3. *Ophthalmology.* 2018;125(4):537-548.
28. Ambati J, Anand A, Fernandez S, et al. An animal model of age-related macular degeneration in senescent Ccl-2- or Ccr-2-deficient mice. *Nat Med.* 2003;9(11):1390-1397.
29. Wright CB, Uehara H, Kim Y, et al. Chronic Dicer1 deficiency promotes atrophic and neovascular outer retinal pathologies in mice. *Proc Natl Acad Sci USA.* 2020;117(5):2579-2587.
30. Tarallo V, Hirano Y, Gelfand BD, et al. DICER1 loss and Alu RNA induce age-related macular degeneration via the NLRP3 inflammasome and MyD88. *Cell.* 2012;149(4):847-859.
31. Kim SY, Yang HJ, Chang YS, et al. Deletion of aryl hydrocarbon receptor AHR in mice leads to subretinal accumulation of microglia and RPE atrophy. *Invest Ophthalmol Vis Sci.* 2014;55(9):6031-6040.
32. Karan G, Lillo C, Yang Z, et al. Lipofuscin accumulation, abnormal electrophysiology, and photoreceptor degeneration in mutant ELOVL4 transgenic mice: a model for macular degeneration. *Proc Natl Acad Sci USA.* 2005;102(11):4164-4169.
33. Justilien V, Pang JJ, Renganathan K, et al. SOD2 knock-down mouse model of early AMD. *Invest Ophthalmol Vis Sci.* 2007;48(10):4407-4420.
34. Dawson WW, Dawson JC, Lake KP, Gonzalez-Martinez J. Maculas, monkeys, models, AMD and aging. *Vision Res.* 2008;48(3):360-365.
35. El-Mofty A, Gouras P, Eisner G, Balazs EA. Macular degeneration in rhesus monkey (*Macaca mulatta*). *Exp Eye Res.* 1978;27(4):499-502.
36. Yiu G, Tieu E, Munevar C, et al. In vivo multimodal imaging of drusenoid lesions in rhesus macaques. *Sci Rep.* 2017;7(1):15013.
37. Yiu G, Chung SH, Mollhoff IN, et al. Long-term evolution and remodeling of soft drusen in rhesus macaques. *Invest Ophthalmol Vis Sci.* 2020;61(2):32.
38. Tran TM, Kim S, Lin KH, et al. Quantitative fundus autofluorescence in rhesus macaques in aging and age-related drusen. *Invest Ophthalmol Vis Sci.* 2020;61(8):16.
39. Bhutto IA, Ogura S, Baldeosingh R, McLeod DS, Luttly GA, Edwards MM. An acute injury model for the phenotypic characteristics of geographic atrophy. *Invest Ophthalmol Vis Sci.* 2018;59(4):AMD143-AMD151.
40. Shirai H, Mandai M, Matsushita K, et al. Transplantation of human embryonic stem cell-derived retinal tissue in two primate models of retinal degeneration. *Proc Natl Acad Sci USA.* 2016;113(1):E81-90.
41. Lorach H, Kung J, Beier C, et al. Development of animal models of local retinal degeneration. *Invest Ophthalmol Vis Sci.* 2015;56(8):4644-4652.
42. Hadziahmetovic M, Kumar U, Song Y, et al. Microarray analysis of murine retinal light damage reveals changes in iron regulatory, complement, and antioxidant genes in the neurosensory retina and isolated RPE. *Invest Ophthalmol Vis Sci.* 2012;53(9):5231-5241.
43. Ding Y, Aredo B, Zhong X, Zhao CX, Ufret-Vincenty RL. Increased susceptibility to fundus camera-delivered light-induced retinal degeneration in mice deficient in oxidative stress response proteins. *Exp Eye Res.* 2017;159:58-68.
44. Ghosn C, Almazan A, Decker S, Burke JA. Brimonidine drug delivery system (Brimo DDS Generation 1) slows the growth of retinal pigment epithelial hypofluorescence following regional blue light irradiation in a nonhuman primate (NHP) model of geographic atrophy (GA). *Invest Ophthalmol Vis Sci.* 2017;58(8):1960-1960.
45. Odergren A, Ming Y, Kvanta A. Photodynamic therapy of experimental choroidal neovascularization in the mouse. *Curr Eye Res.* 2006;31(9):765-774.
46. Adhi M, Lau M, Liang MC, Waheed NK, Duker JS. Analysis of the thickness and vascular layers of the choroid in eyes with geographic atrophy using spectral-domain optical coherence tomography. *Retina.* 2014;34(2):306-312.
47. Capuano V, Souied EH, Miere A, Jung C, Costanzo E, Querques G. Choroidal maps in non-exudative age-related macular degeneration. *Br J Ophthalmol.* 2016;100(5):677-682.

48. Lindner M, Bezatis A, Czauderna J, et al. Choroidal thickness in geographic atrophy secondary to age-related macular degeneration. *Invest Ophthalmol Vis Sci.* 2015;56(2):875–882.
49. Seddon JM, McLeod DS, Bhutto IA, et al. Histopathological insights into choroidal vascular loss in clinically documented cases of age-related macular degeneration. *JAMA Ophthalmology.* 2016;134(11):1272–1280.
50. Pilotto E, Midena E, Longhin E, Parrozzani R, Frisina R, Frizziero L. Müller cells and choriocapillaris in the pathogenesis of geographic atrophy secondary to age-related macular degeneration. *Graefes Arch Clin Exp Ophthalmol.* 2019;257(6):1159–1167.
51. Giani A, Pellegrini M, Carini E, Peroglio Deiro A, Bottoni F, Staurengi G. The dark atrophy with indocyanine green angiography in Stargardt disease. *Invest Ophthalmol Vis Sci.* 2012;53(7):3999–4004.
52. Alabduljalil T, Patel RC, Alqahtani AA, et al. Correlation of outer retinal degeneration and choriocapillaris loss in Stargardt disease using en face optical coherence tomography and optical coherence tomography angiography. *Am J Ophthalmol.* 2019;202:79–90.
53. Arrigo A, Grazioli A, Romano F, et al. Choroidal patterns in Stargardt disease: correlations with visual acuity and disease progression. *J Clin Med.* 2019;8(9):1388.
54. Bonilha VL, Rayborn ME, Bell BA, Marino MJ, Fishman GA, Hollyfield JG. Retinal histopathology in eyes from a patient with Stargardt disease caused by compound heterozygous ABCA4 mutations. *Ophthalmic Genet.* 2016;37(2):150–160.
55. Muller PL, Pfau M, Moller PT, et al. Choroidal flow signal in late-onset Stargardt disease and age-related macular degeneration: an OCT-angiography study. *Invest Ophthalmol Vis Sci.* 2018;59(4):Amd122–amd131.
56. Ratra D, Tan R, Jaishankar D, et al. Choroidal structural changes and vascularity index in Stargardt disease on swept source optical coherence tomography. *Retina.* 2018;38(12):2395–2400.
57. Sodi A, Bacherini D, Lenzetti C, et al. EDI OCT evaluation of choroidal thickness in Stargardt disease. *PLoS One.* 2018;13(1):e0190780.
58. Wei X, Mishra C, Kannan NB, et al. Choroidal structural analysis and vascularity index in retinal dystrophies. *Acta Ophthalmol.* 2019;97(1):e116–e121.
59. Petrus-Reurer S, Bartuma H, Aronsson M, et al. Integration of subretinal suspension transplants of human embryonic stem cell-derived retinal pigment epithelial cells in a large-eyed model of geographic atrophy. *Invest Ophthalmol Vis Sci.* 2017;58(2):1314–1322.
60. Picaud S, Dalkara D, Marazova K, Goureau O, Roska B, Sahel JA. The primate model for understanding and restoring vision. *Proc Natl Acad Sci USA.* 2019;116(52):26280–26287.
61. Mattison JA, Vaughan KL. An overview of nonhuman primates in aging research. *Exp Gerontol.* 2017;94:41–45.
62. Lin X, Wang Q, He M. Repeated retinal photocoagulation in monkeys for the optimization of a laser-induced choroidal neovascularization model. *Exp Eye Res.* 2019;184:1–7.
63. Lukason M, DuFresne E, Rubin H, et al. Inhibition of choroidal neovascularization in a nonhuman primate model by intravitreal administration of an AAV2 vector expressing a novel anti-VEGF molecule. *Mol Ther.* 2011;19(2):260–265.
64. Anger EM, Unterhuber A, Hermann B, et al. Ultrahigh resolution optical coherence tomography of the monkey fovea. Identification of retinal sublayers by correlation with semithin histology sections. *Exp Eye Res.* 2004;78(6):1117–1125.
65. Yiu G, Wang Z, Munevar C, et al. Comparison of chorioretinal layers in rhesus macaques using spectral-domain optical coherence tomography and high-resolution histological sections. *Exp Eye Res.* 2018;168:69–76.
66. Tan B, Chua J, Barathi VA, et al. Quantitative analysis of choriocapillaris in non-human primates using swept-source optical coherence tomography angiography (SS-OCTA). *Biomed Opt Express.* 2018;10(1):356–371.
67. Coupland S, Tsang A, Gottlieb C, Gostimir M, Dollin M, Nithinandan H. Detecting hydroxychloroquine retinal toxicity using a novel multifocal electroretinography stimulus. *Acta Ophthalmol (Copenh).* 2019;97(S263).
68. Ibbett P, Goverdhan SV, Pipi E, et al. A lasered mouse model of retinal degeneration displays progressive outer retinal pathology providing insights into early geographic atrophy. *Sci Rep.* 2019;9(1):7475.
69. Ronan S, Nusinowitz S, Swaroop A, Heckenlively JR. Senile panretinal cone dysfunction in age-related macular degeneration (AMD): a report of 52 amd patients compared to age-matched controls. *Trans Am Ophthalmol Soc.* 2006;104:232–240.
70. Ebnetter A, Jaggi D, Abegg M, Wolf S, Zinkernagel MS. Relationship between presumptive inner nuclear layer thickness and geographic atrophy progression in age-related macular degeneration. *Invest Ophthalmol Vis Sci.* 2016;57(9):Oct299–306.
71. Fleckenstein M, Schmitz-Valckenberg S, Adrion C, et al. Tracking progression with spectral-domain optical coherence tomography in geographic atrophy caused by age-related macular degeneration. *Invest Ophthalmol Vis Sci.* 2010;51(8):3846–3852.
72. Sacconi R, Corbelli E, Carnevali A, Querques L, Bandello F, Querques G. Optical coherence tomography angiography in geographic atrophy. *Retina.* 2018;38(12):2350–2355.
73. Sohn EH, Flamme-Wiese MJ, Whitmore SS, et al. Choriocapillaris degeneration in geographic atrophy. *Am J Pathol.* 2019;189(7):1473–1480.
74. Whitmore SS, Sohn EH, Chirco KR, et al. Complement activation and choriocapillaris loss in early AMD: implications for pathophysiology and therapy. *Prog Retin Eye Res.* 2015;45:1–29.
75. Friedman E, Krupsky S, Lane AM, et al. Ocular blood flow velocity in age-related macular degeneration. *Ophthalmology.* 1995;102(4):640–646.
76. Grebe R, Mughal I, Bryden W, et al. Ultrastructural analysis of submacular choriocapillaris and its transport systems in AMD and aged control eyes. *Exp Eye Res.* 2019;181:252–262.
77. McLeod DS, Taomoto M, Otsuji T, Green WR, Sunness JS, Luty GA. Quantifying changes in RPE and choroidal vasculature in eyes with age-related macular degeneration. *Invest Ophthalmol Vis Sci.* 2002;43(6):1986–1993.
78. Pellegrini M, Acquistapace A, Oldani M, et al. Dark atrophy: an optical coherence tomography angiography study. *Ophthalmology.* 2016;123(9):1879–1886.
79. Terrell D, Comander J. Current stem-cell approaches for the treatment of inherited retinal degenerations. *Semin Ophthalmol.* 2019;34(4):287–292.
80. Schwartz SD, Regillo CD, Lam BL, et al. Human embryonic stem cell-derived retinal pigment epithelium in patients with age-related macular degeneration and Stargardt's macular dystrophy: follow-up of two open-label phase 1/2 studies. *Lancet.* 2015;385(9967):509–516.
81. Roider J, Hillenkamp F, Flotte T, Birngruber R. Microphotocoagulation: selective effects of repetitive short laser pulses. *Proc Natl Acad Sci USA.* 1993;90(18):8643–8647.
82. Berger JW. Thermal modelling of micropulsed diode laser retinal photocoagulation. *Lasers Surg Med.* 1997;20(4):409–415.
83. Song Q, Risco R, Latina M, Berthiaume F, Nahmias Y, Yarmush ML. Selective targeting of pigmented retinal pigment epithelial (RPE) cells by a single pulsed laser

- irradiation: an in vitro study. *Opt Express*. 2008;16(14):10518–10528.
84. Pollack A, Korte GE. Choroidal vascular repair: scanning and transmission electron microscopy. *Experientia*. 1992;48(3):219–225.
85. Korte GE. Choriocapillaris regeneration in the rabbit. Ultrastructure of new endothelial tube formation. *Invest Ophthalmol Vis Sci*. 1989;30(9):1938–1950.
86. Bouskila J, Palmour RM, Bouchard JF, Ptito M. Retinal structure and function in monkeys with fetal alcohol exposure. *Exp Eye Res*. 2018;177:55–64.
87. Augsburger AS, Haag V, Leuillet S, Legrand JJ, Forster R. Recording of the full-field electroretinogram in minipigs. *Vet Ophthalmol*. 2012;15(Suppl 2):84–93.
88. Chong NHV, Keonin J, Luthert PJ, et al. Decreased thickness and integrity of the macular elastic layer of Bruch's membrane correspond to the distribution of lesions associated with age-related macular degeneration. *Am J Pathol*. 2005;166(1):241–251.
89. Biesemeier A, Yoeruek E, Eibl O, Schraermeyer U. Iron accumulation in Bruch's membrane and melanosomes of donor eyes with age-related macular degeneration. *Exp Eye Res*. 2015;137:39–49.
90. Edwards MM, McLeod DS, Bhutto IA, Grebe R, Duffy M, Luty GA. Subretinal glial membranes in eyes with geographic atrophy. *Invest Ophthalmol Vis Sci*. 2017;58(3):1352–1367.
91. Chidlow G, Shibebe O, Plunkett M, Casson RJ, Wood JP. Glial cell and inflammatory responses to retinal laser treatment: comparison of a conventional photocoagulator and a novel, 3-nanosecond pulse laser. *Invest Ophthalmol Vis Sci*. 2013;54(3):2319–2332.
92. Shiragami C, Matsuo T, Shiraga F, Matsuo N. Transplanted and repopulated retinal pigment epithelial cells on damaged Bruch's membrane in rabbits. *Br J Ophthalmol*. 1998;82(9):1056–1062.
93. Gullapalli VK, Sugino IK, Van Patten Y, Shah S, Zarbin MA. Impaired RPE survival on aged submacular human Bruch's membrane. *Exp Eye Res*. 2005;80(2):235–248.